Korean J. Chem. Eng., 40(9), 2102-2118 (2023)
DOI: 10.1007/s11814-023-1493-0

pISSN: 0256-1115
eISSN: 1975-7220

Activated carbon from municipal waste for enhanced CO_2/CH_4 membrane separation: Experimental, modeling and simulation

Abolfazl Jomekian*,† and Bahamin Bazooyar**

*Esfarayen University of Technology, Esfarayen, North Khorasan, Iran
**Department of Mechanical, Aerospace and Civil Engineering (MACE), The University of Manchester, Manchester, M13 9PL, UK
(*Received 29 October 2022 • Revised 30 March 2023 • Accepted 8 May 2023*)

Abstract−Three conventional and abundant municipal wastes (PET bottles, bread, and human hair) were used for the synthesis of the solid carbon product. The activation of this carbon powder was performed with the aid of KOH and $ZnCl_2$ chemicals to achieve activated carbons (ACs). The characterization methods, such as SEM, FTIR, N_2 adsorption-desorption analysis, BET, and DFT pore size analysis, were applied to characterize the synthesized mixed matrix membranes (MMMs). The ACs synthesized by PET wastes and human hairs showed the highest and lowest sorption capacity, BET surface area, and pore volume, respectively. The activation of ACs using KOH showed overall better effectiveness in CO_2/CH_4 separation performance of fabricated MMMs compared with using $ZnCL_2$, due to the presence of hydroxyl groups at the surface of KOH-modified ACs. The developed model for the spiral wound membrane module showed good agreement with experimental data and modeling results of the hollow fiber module in the literature. The result of the model on the best-performed membrane showed that the increase in module length and diameter led to a logarithmic increase in the stage cut. It appears that the increase in module diameter is more practical and beneficial than that in module length. The result of the simulation of a double step with recycling of permeate (DoSRP) separation system in the Aspen Plus environment shows that the increase in CH_4 content of the feed, temperature, and decrease in thickness of membranes all have deteriorative effect on the separation performance of overall DoSRP configuration separation system. It was also deduced that MMMs with higher CO_2 permeance and CO_2/CH_4 ideal selectivity suffer more from the mentioned changes in simulated manipulated separation parameters compared with less effective MMMs.

Keywords: Municipal Wastes, Activated Carbon, Polyvinyl Alcohol, Mixed Matrix Membrane, CO_2, CH_4

INTRODUCTION

The production rate of municipal solid wastes (MSW) has increased dramatically in the recent decade mostly due to the rapid population growth in cities and the alteration of people's lifestyles, especially in developing countries. These wastes are mostly generated from domestic, industrial, and commercial parts of cities. MSW mainly includes food waste, plastic waste, and biological waste. In Iran, about 25 million tons of MSW waste is generated every day [1] with a composition of 68.4% for organic materials, including food and biological wastes, and 9.8% for plastic wastes, and 21.8% for other types of waste [2]. This tremendous amount of generated MSW has motivated researchers to look for a variety of waste-managing methods and plans, such as landfilling [3], composting [4], anaerobic digestion [5], fuel production from wastes [6], and thermal processes [7]. One of the most promising methods of MSW management is to convert these wastes to high-tech adsorbents, such as activated carbons (AC)s, by thermal methods [8]. This adsorbent can be synthesized from all three main types of MSWs [9,10] and thermal processes such as combustion and pyrolysis have been used extensively for this purpose. AC with high surface area and pore volume, applicable microporosity, and long life span is one of the more favorite carbon-based materials for the adsorption of hazardous vapors and gases such as CO_2, CO, and H_2S [11, 12]. CO_2 is known to be the source of many industrial and environmental problems. Pipeline corrosion, hydrate formation in natural gas transmission, and global warming are widely known ones. The capture of this gas by cost-effective and efficient methods is of great interest, hence membrane processes are suggested as one of the most attractive methods of CO_2 separation. Investigations on the various inorganic, polymeric, and mixed matrix membranes (MMMs) for CO_2 separation have been developed to a large extent, especially in the last twenty years. Multilayer MMMs with a combined thin selective layer and a porous thick sub-layer showed effectiveness in CO_2 separation [13,14]. The selection of materials, design of configurations and modules, and determination of the concentration of solutions to fabricate selective layers are of the utmost importance in the synthesis of mixed matrix membranes. Moreover, the cost of large-scale synthesis of industrially attractive membranes for gas separation has to be as low as possible, provided that the gas separation performance of the membrane is not compromised. It is clear that the utilization of laboratory-grade effective car-

†To whom correspondence should be addressed.
E-mail: abolfazl.jomekian@gmail.com, a_jomekian@esfarayen.ac.ir

bon-based fillers in the matrix of polymers is a very expensive practice and their use as precursors for large-scale synthesis of MMMs is not economically attractive. For instance, any lab-grade graphene, single-walled and multi-walled carbon nanotube costs more than $ 50,000/kg [15] or lab-grade AC powder costs more than $ 73/kg [16]. Therefore, it is important for large-scale production membrane separation plants to find cheap, accessible and effective raw materials for the fabrication of membranes. Accordingly, to make our study both an environmentally and economically attractive work, we decided to utilize wasted food materials as cheap precursors for production of ACs (with estimated cost of about $ 15/kg) and polyvinyl alcohol (PVA) as the polymeric base of the membrane because it is also a cheap and widely accessible polymer with excellent film-forming ability, remarkable flexibility, high mechanical stability, and tensile strength. It has also confirmed resistance against hydrophobic materials but shows susceptibility toward water and moisture [17]. Remarkable works on the separation performance of this polymer blended with other polymers, inorganic or organic fillers have been reported in recent years. Barooah and Mandal [18] synthesized and examined ZIF-8/PVA/PEG mixed matrix membrane for the CO_2/N_2 separation. They reported relatively high CO_2 permeance with significantly enhanced CO_2/N_2 selectivity. Torstensen et al. [19] reported the fabrication and performance investigation of PVA/nanocellulose MMMs for the separation of CO_2 from flue gas. In their work, the permeance of CO_2 and the CO_2/N_2 selectivity of synthesized MMMs showed a slight improvement compared with pristine PVA membranes. The same material (PVA/nanocellulose) was tried by Jahan et al. [20] for the preparation of MMMs. They concluded that PVA/nanocellulose facilitated transport MMMs are notably superior to PVA regarding CO_2 permeance and CO_2/CH_4 selectivity. Guerrero et al. [21] synthesized amino modified polyhedral oligomeric silsesquioxane (POSS)/PVA MMMs for CO_2/N_2 separation. They reported that POSS could not satisfy the expectation for increase in CO_2 permeance due to the undesirable interaction of POSS with PVA; however, polypropylene oxide (PPO)/PVA membrane in their work showed improvement in separation performance over PVA membrane.

Therefore, in the experimental part of this study as a new approach, three types of most common MSW were selected for the synthesis of ACs. Human hair, bread, and PET plastic wastes, which are among the most observed and reported MSW in Iran, were selected as three different precursors for ACs synthesis. The resulting AC samples were separately introduced in the matrix of PVA to yield AC/PVA MMMs. SEM, FTIR, N_2 adsorption-desorption analyses, BET surface area measurement, and density functional theory (DFT) pore size profile analysis were utilized to characterize the prepared AC powder and prepared MMMs. Pure gas permeation tests were applied to evaluate the performance of synthesized MMMs for the separation of CO_2 from CH_4. The results of permeation experiments were used as input for the modeling and simulation part of the work, which is focused on the presentation of a permeation model for spiral wound membrane modules that accurately predict the separation performance of membranes and a sensitivity analysis of evaluation of the effect of different feed properties and operating parameters on the performance of a double stage membrane separation system.

EXPERIMENTAL

1. Materials

Human hair, bread (Mazraeh®), and PET bottles were supplied from domestic waste. Hydrochloric acid (HCl, 36%) and polyvinyl alcohol (PVA) were purchased from Merck Inc. Aqueous solution of ammonia (30 wt%), deionized water, hexadecyl trimethylammonium bromide (CTAB, 99.5%), zinc chloride ($ZnCl_2$, 99.90%), (N, N-Dimethylformamide (DMF, 99.98%) and potassium hydroxide (KOH, 98%) were supplied from Sigma-Aldrich and used without further purification.

2. Synthesis of Carbon Powder and Activation Procedure

2 g of each precursor (hair, bread, and PET wastes) was separately stirred with 0.5 mL of aqueous ammonia and 0.06 g of CTAB for 4 h. The resulting mixture was filtered and then poured into a Teflon-lined autoclave, which was then placed in an oven for 5 h at 270 °C. The resulting powder was washed twice with deionized water and twice with ethanol, and then centrifuged and dried in air at 50 °C for 12 hours. The resulting powder is arbitrarily called the "raw carbon particles" and abbreviated with (RCP).

To activate RCPs with $ZnCl_2$, 1 g of resulting RCP was mixed with $ZnCl_2$ with the mass ratio of RCP/$ZnCl_2$=1/1 and 50 mL of water. The mixture was stirred at 50 °C for 2 h and then dried for 24 h in the oven at 90 °C. The resulting sample was placed in a furnace adjusted to raise the temperature at a rate of 5 °C/min from 25 °C to 350 °C and then from 350 °C to 800 °C. The temperature rises halted twice, once at 350 °C and once at 800 °C each for 2 h.

To activate RCPs with KOH, 1 g of RCP was stirred with KOH with the mass ratio of RCP/KOH=1/1 and 30 mL of water. The rest of the procedure was exactly similar to the procedure of activation with $ZnCl_2$ with the only change in the maximum temperature of calcination from 800 °C to 600 °C.

Finally, both versions of activated samples were completely washed with an aqueous solution of HCl (1 M) and deionized water, and then centrifuged and dried at 50 °C for 12 hours. The samples were placed in a crucible and ground in mortar for 1 h.

3. Synthesis of AC/PVA Mixed Matrix Membrane

To synthesize the casting solution of MMMs, 4 g of PVA was stirred in 90 ml of deionized water at 60 °C for 4 h. 0.5 g of AC powder was suspended in 10 ml of deionized water followed by vigorous stirring for 2 h. The resulting suspension was added to the PVA solution then successive operations of 15 min of sonication and 30 min of stirring were applied to the MMM solution (3 cycles). The resulting sample was aged for 2 h for bubble removal. To achieve a uniform selective layer for a dense membrane, the solution casting method was applied. A flat rectangle-shaped piece of glass was selected as casting support. An adjustable casting knife was used to cast the prepared solution on the surface of the glass. The gap between the casting knife blades was set to 100 μm. The casting procedure was performed as gently and as uniformly as possible. The glass held its position after casting for 48 h for solvent (water) evaporation. The cast film, which is our targeted MMM, was removed from the glass and maintained in a clean environment to be evaluated in permeation experiments. The code names of the prepared samples in this study along with the preparation parameters are provided in Table 1.

Table 1. The code names of synthesized and modified MMMs with different waste precursors and activation chemicals

Code names of membranes	Precursor for AC	Activator of RCPs
H-AC/PVA-Z	Hair	$ZnCl_2$
B-AC/PVA-Z	Bread	$ZnCl_2$
P-AC/PVA-Z	PET	$ZnCl_2$
H-AC/PVA-K	Hair	KOH
B-AC/PVA-K	Bread	KOH
P-AC/PVA-K	PET	KOH
PVA	-	-

4. CO_2 and CH_4 Permeance Measurements

The permeances of CO_2 and CH_4 were measured using a flat PTFE membrane module equipped with a bubble flowmeter. The CO_2 and CH_4 gas capsules containing gases with 99.99% purity were used as the feed of membranes (Fig. 1).

The permeances of CO_2 and CH_4 were calculated based on the following formula:

$$P_i = \frac{Q_i}{A(p_{f_i} - p_{p_i})} \tag{1}$$

where P_i is the symbol for permeance (cm^3 (STP) s^{-1} cm^{-2} $cmHg^{-1}$) of gas i, Q_i is the volumetric flowrate of gas i in the permeate stream (cm^3 (STP) s^{-1}), A is permeable membrane area (cm^2), and p_{p_i} is permeate side pressure and p_{f_i} is feed side pressures of gas i (cmHg).

Dividing the permeance of more permeable penetrant (A) to that of less permeable penetrant (B) leads to the definition of the ideal selectivity $\alpha_{A/B}$ by the following formula:

$$\alpha_{A/B} = \frac{P_A}{P_B} \tag{2}$$

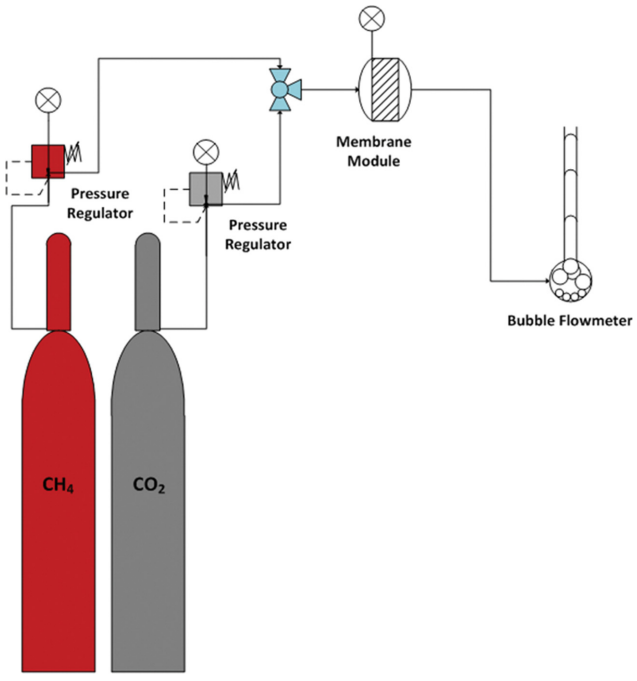

Fig. 1. Schematic diagram and image of applied gas permeation set-up with an embedded image of the utilized membrane module.

5. Characterization

To investigate the morphology of the cross-section of membranes in two different levels of magnifications together with the surface morphology of the membranes, a scanning electron microscope (SEM) (TESCAN-MIRA3) was used. The FT-IR (IRAffinity-1S, Shimadzu) spectra for the identification of new formation of functional groups at the surface of the fabricated membranes with an average of eight scans in the range of 400-4,000 cm^{-1} were applied. The volumetric measurement approach at pressure up to 1 bar and the temperature of 77 K was adapted to determine the adsorption isotherms for all samples. About 0.15 g of each considered sample was separated and applied in the determination of each isotherm at 70 °C for about 120 min of vacuum, which was exerted on every membrane before the test for the sake of confidence that the pores of the sample were empty. The BET method was used for the calculation of the BET surface area of membranes using the obtained data in the range of $0.02<P/P_0<0.2$ from the corresponding isotherm. The pore size profile of membranes was measured following density functional theory using specific software provided by the Micromeritics (ASAP 2020). The appropriateness of fit with the adjustment parameter of 0.01 was selected as a reference point for the simulation. Operation of some characterization items can refer to the literature [22-25].

MODELING AND SIMULATIONS

The solution-diffusion mechanism, which is an established and widely trusted model for defining the permeation through the membrane, was regarded as the foundation of the modeling in this study. If Eq. (1) is expressed with more detail for j numbers of penetrants, the resulting equation becomes as follows:

$$J_j = \frac{y_j Q}{A} = P_j[p_f x_j - p_p y_j] \tag{3}$$

where x_j is the mole fraction of component j in feed or retentate stream and y_j is the mole fraction of component j in permeate stream.

For a two-component feed (e.g. CO_2 and CH_4) the above equation can be turned into the following equation using division:

$$\frac{y_{CO_2}}{y_{CH_4}} = \alpha \frac{p_f x_{CO_2} - p_p y_{CO_2}}{p_f x_{CH_4} - p_p y_{CH_4}} \tag{4}$$

where α is the CO_2/CH_4 selectivity of the membrane.

Rearranging Eq. (4) yields a quadratic algebraic equation:

$$\left(\frac{p_p}{p_f} + \alpha(p_f - p_p)\right) y_{CO_2}^2 + \left(\alpha x_{CO_2} + 1 - x_{CO_2} - \frac{p_p}{p_f} - \alpha(p_f - p_p)\right) y_{CO_2} - \alpha x_{CO_2} = 0 \tag{5}$$

Solving Eq. (5) gives y_{CO_2} and thereafter the flux through a small flat sheet module (J). However, due to the limitation of the effective surface area of a flat membrane module, it is not possible to use these types of modules for industrial or pilot membrane sys-

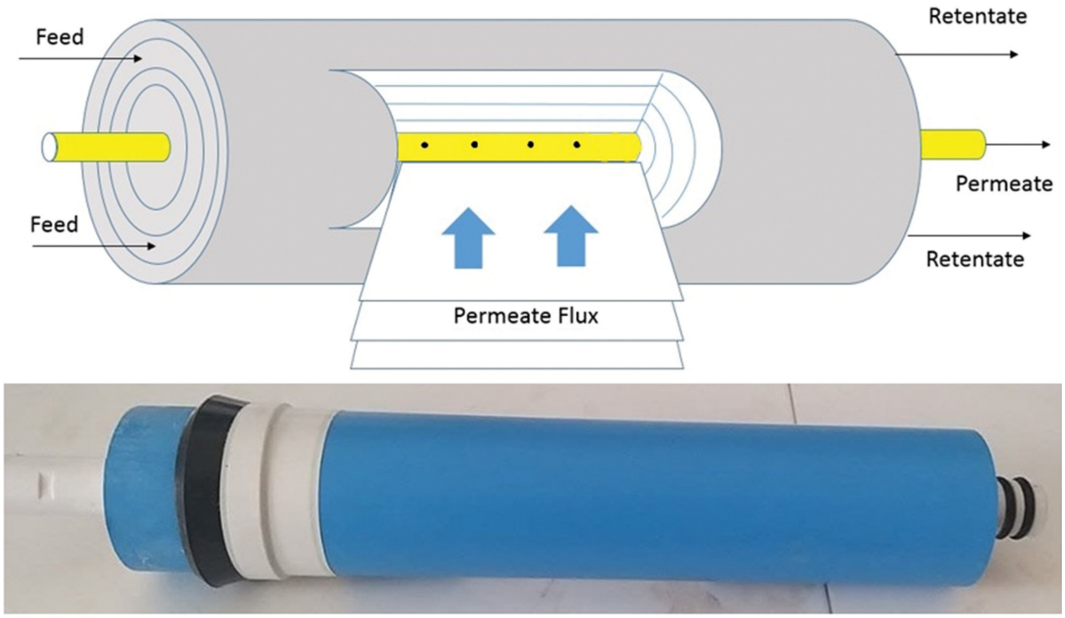

Fig. 2. Schematic image of the spiral-wound module with its detailed flows (up) and the image of the utilized spiral-wound module (down).

tems. The solution to this issue is to modulate flat sheet membranes into a more effective spiral-wound module with a much higher surface area. To do that, a spiral wound model was developed based on mass balance over the spaces between membrane sheets (Fig. 2).

As can be observed in this figure, the permeated flux through the membrane is divided into two parts. One is related to permeates of even spacers and the other is related to odd spacers based on the following relationships derived from the solution-diffusion mechanism:

$$\text{for even n: } J_{n,i} = P_{n,i}\left(p_{r,\left(\frac{n}{2}\right)} \times x_{\left(\frac{n}{2}\right),i} - p_{p,\left(\frac{n}{2}+1\right)} \times y_{\left(\frac{n}{2}+1\right),i}\right)A \quad (6)$$

$$\text{for odd n: } J_{n,i} = P_{n,i}\left(p_{r,\left(\frac{n+1}{2}\right)} \times x_{\left(\frac{n+1}{2}\right),i} - p_{p,\left(\frac{n+1}{2}\right)} \times y_{\left(\frac{n+1}{2}\right),i}\right)A \quad (7)$$

where $J_{n,i}$ is the flux of component i through the membrane in n^{th} channel (mol m^{-2} s^{-1}), $P_{n,i}$ is the permeance of component i through the membrane in n^{th} channel (mol m^{-2} s^{-1}), $p_{r,(n/2)}$ and $p_{r,(n+1/2)}$ are retentate side pressure of i component in channels of n/2 and (n+1)/2, respectively (Pa). Similarly, $p_{p,(n/2+1)}$ and $p_{p,(n+1/2)}$ are permeate side pressure of i component in channels of n/2+1 and (n+1)/2, respectively (Pa). x_i and y_i are the composition of i component in corresponding channels shown by subscribed notation. A is the area of membrane in each channel (m^2) which is calculated by the following relationship:

$$A = \pi(D_0 + 2n \times \delta_{ch})L \quad (8)$$

where D_0 is the diameter of the central pipe of the module for integration of permeates (m), δ_{ch} is the thickness of the spacer between two adjacent layers of membranes (m) and L is the length of the membrane (m) inside the module.

The following assumptions were made to derive mass balance equations for the spiral wound membrane module:

1- Membrane separation properties (permeance and selectivity) are constant at the pressure and the temperature of the process.

2- There is negligible mass transfer resistance in the gas phase on either side of the membrane.

3- The membrane's physical structure maintains its integrity during the separation process.

4- The system is in steady-state condition.

The flowchart presented in Fig. 3 indicates the incremental cal-

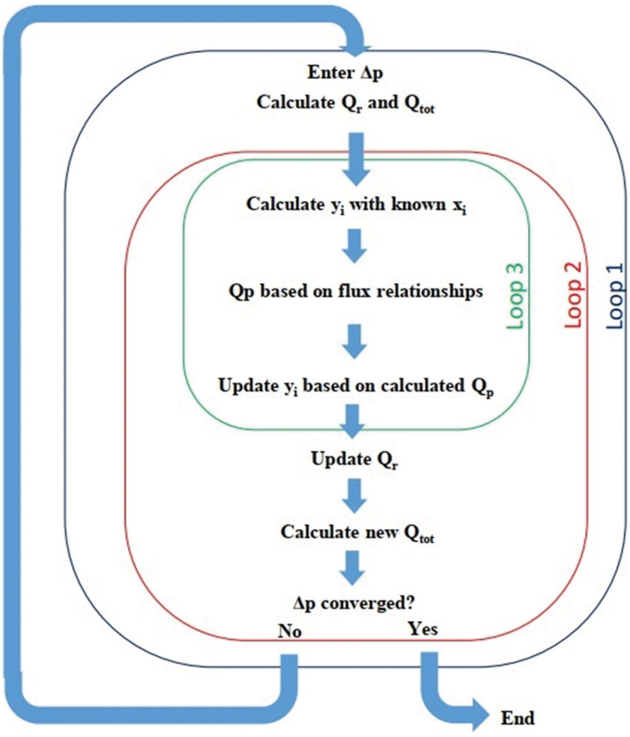

Fig. 3. Illustration of iterative calculation procedures of the developed model.

culations and iterations for the determination of compositions of CO_2 and CH_4 in the retentate and permeate side of the module.

As can be seen in this figure, the calculation procedure consists of three nested loops. Loop 1 reinitializes the trial and error process by changing the initial guess for pressure drop across the membrane. Loop 2 integrates along the length of the membrane to determine the composition and flow rate of the permeate in each channel. Loop 3 solves the mass and momentum balances for each discretized stage iteratively until convergence occurs.

In the first step, a constant pressure drop (Δp) across the membrane is considered. The value for the pressure drop can be changed from 10 kPa to 50 kPa (conventional pressure drop for spiral wound gas separation membranes) to achieve CO_2 composition in the range of 1% to 20%. The iteration approach was selected to determine the correct value for (Δp) by calculation of the flow rate of each channel. The initial assumed (Δp) was used to calculate the initial value for total feed flowrate based on a relationship presented by Gurreri et al. [26]:

$$\Delta p = \frac{12\mu L}{\delta_{ch}^3 \rho W} Q_{totk_r} \tag{9}$$

where W is the width of the membrane (m), is the density of the feed gas mixture ρ (mol·m^{-3}), μ is the viscosity of the feed gas mixture (Pa·s), δ_{ch} is the spacer or channel gap (m), and k_r is a subscribed notation for the retentate channel number. Based on this relationship, the friction factor is introduced as:

$$\lambda = \frac{12\mu L}{\delta_{ch}^3 \rho W} \tag{10}$$

where the density and viscosity of the mixture are calculated as follows [27]:

$$\rho = x_{CO_2}\rho_{CO_2} + (1 - x_{CO_2})\rho_{CH_4} \tag{11}$$

$$\mu = \sum_{i=1}^{C} \frac{x_i \mu_i}{\sum_{k=1}^{C} x_k \varphi_{ik}} \tag{12}$$

In which

$$\varphi_{ik} = \frac{1}{\sqrt{8}}\left(1 + \frac{M_i}{M_k}\right)^{-1/2}\left[1 + \left(\frac{\mu_i}{\mu_k}\right)^{1/2}\left(\frac{M_i}{M_k}\right)^{1/2}\right]^2 \tag{13}$$

where

$$\mu_i = 2.6693 \times 10^{-5} \frac{\sqrt{M_i T}}{\sigma_i^2 \Omega_i} \tag{14}$$

where M_i is the molecular weight of component i, σ_i is the Lennard Jones potential parameter for component i, and Ω_i is the collision integral of component i.

Therefore, we have:

$$\Delta p = \lambda Q_{totk_r} \tag{15}$$

Then, the feed flow rate is used to calculate the component flows in the feed, $Q_{kr,i}$ (mol·s^{-1}), with the aid of the known feed composition, z_i, as shown in Eq. (4):

$$Q_{k_r, CO_2} = z_{CO_2} Q_{totk_r} \tag{16}$$

$$Q_{k_r, CH_4} = (1 - z_{CO_2}) Q_{totk_r} \tag{17}$$

The above-calculated flow rates of components in retentate channels are the initial values of these parameters that have to enter the inner loop (loop 2) for the integration of flowrates in all channels and provide an overall flow rate of permeate and retentate. The next step is to establish mass balance equations to solve for the change in gas concentration along the length of the membrane, and in order to do that, the membrane length is divided into a series of n stages (n is determined based on the length of membrane and the accuracy needed), as indicated in Fig. 4.

Because each permeate channel is fed from its two adjacent retentate channels, an iterative approach is required for the calculation of the permeate composition in each channel. The first and last channels are exceptions because they are only fed from one retentate channel. A scheme of how it is modeled is presented in Fig. 5.

For the calculation of permeate composition in each channel at stage 1, the feed composition is used:

$$y_{k_p, CO_2} = z_{CO_2} \tag{18}$$

$$y_{k_p, CH_4} = 1 - z_{CO_2} \tag{19}$$

Using the first guesses for mole fractions of permeates, the permeate flow rates of CO_2 and CH_4 are calculated as the sum of the CO_2 permeate flows and CH_4 permeate flows from the two neighbor-

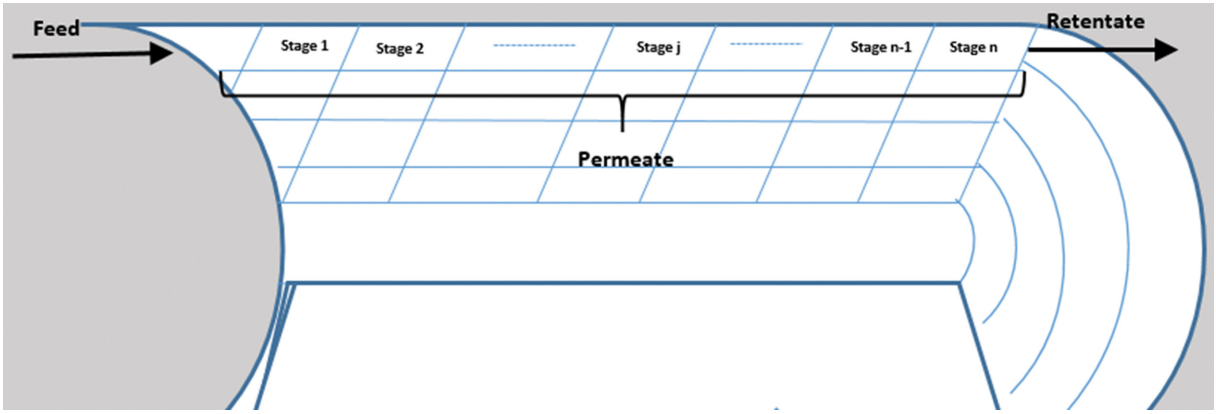

Fig. 4. Discretized membrane module into n segments along the length of a retentate channel.

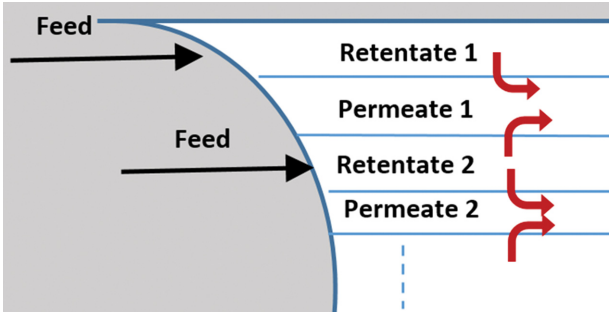

Fig. 5. Illustration of how each permeate channel is fed with its two adjacent retentate channels.

ing retentate channels:

$$Q_{k_p,\,CO_2} = P_{CO_2,\,u}(p_{H,\,u}x_{CO_2,\,u} - p_{L,\,k_p}y_{k_p,\,CO_2}) + P_{CO_2,\,l}(p_{H,\,l}x_{CO_2,\,l} - p_{L,\,k_p}y_{k_p,\,CO_2}) \quad (20)$$

$$Q_{k_p,\,CH_4} = P_{CH_4,\,u}(p_{H,\,u}(1-x_{CO_2,\,u}) - p_{L,\,k_p}(1-y_{k_p,\,CO_2})) + P_{CH_4,\,l}(p_{H,\,l}(1-x_{CO_2,\,l}) - p_{L,\,k_p}(1-y_{k_p,\,CO_2})) \quad (21)$$

where Q_{k_p,CO_2} and Q_{k_p,CH_4} are permeate flowrates of CO_2 and CH_4 in channel k_p, respectively (mol·s^{-1}). P_{CO_2} and P_{CH_4} are the permeance of CO_2 and CH_4 passing through the membrane, respectively. P_H and P_L are high and low pressure across the module which are, respectively, related to feed and permeate pressures. The subscribed notations of u and *l* are related to the upper and lower channels respected to k_p permeate channel, respectively.

y_{k_p} values for CO_2 and CH_4 are updated based on the following estimating relationship:

$$y_{k_p,\,CO_2} = \frac{Q_{k_p,\,CO_2}}{Q_{k_p,\,CO_2} + Q_{k_p,\,CH_4}} \quad (22)$$

$$y_{k_p,\,CH_4} = \frac{Q_{k_p,\,CH_4}}{Q_{k_p,\,CO_2} + Q_{k_p,\,CH_4}} \quad (23)$$

For the permeate channels at channels adjacent to the inner and outer walls of the module, the permeate gathers from only one adjacent retentate channel hence there is a slight modification in the relationship for the calculation of permeate compositions in these channels:

$$y_{i,\,1} = \frac{P_{i,\,1}(p_{H,\,1}x_{i,\,1} - p_{L,\,1}y_{1,\,i})}{Q_{ch\,1}} \quad (24)$$

$$y_{\frac{N}{2}+1,\,1} = \frac{P_{\frac{N}{2}+1,\,1}\left(p_{H,\,\frac{N}{2}}x_{i,\,\frac{N}{2}} - p_{L,\,\frac{N}{2}+1}y_{\frac{N}{2}+1,\,i}\right)}{Q_{ch\,\frac{N}{2}+1}} \quad (25)$$

Eqs. (18)-(25) are repeated until the convergence condition with the error tolerance of 1e-6 is met. After the completion of the calculations in this loop, the permeate compositions in each channel are fed back to the middle loop. This data is used for the calculation of retentate channel compositions and flow rates on a per-stage basis.

After the calculation of permeate flowrate and composition, the retentate flowrate of each stage is recalculated based on the revised information of the two adjacent permeate channels respected to the retentate channel (upper and lower channels):

$$Q_{k_r,\,CO_2} = Q_{k_r,\,CO_2} - L_jP_{CO_2,\,u}\left(p_{H,\,k_r}\frac{Q_{k_r,\,CO_2}}{Q_{tot,\,k_r}} - p_{L,\,u}y^*_{CO_2,\,u}\right) - L_jP_{CO_2,\,l}\left(p_{H,\,k_r}\frac{Q_{k_r,\,CO_2}}{Q_{tot,\,k_r}} - p_{L,\,l}y^*_{CO_2,\,l}\right) \quad (26)$$

$$Q_{k_r,\,CH_4} = Q_{k_r,\,CH_4} - L_jP_{CH_4,\,u}\left(p_{H,\,k_r}\frac{Q_{k_r,\,CH_4}}{Q_{tot,\,k_r}} - p_{L,\,u}(1-y^*_{CO_2,\,u})\right) - L_jP_{CH_4,\,l}\left(p_{H,\,k_r}\frac{Q_{k_r,\,CH_4}}{Q_{tot,\,k_r}} - p_{L,\,l}(1-y^*_{CO_2,\,u})\right) \quad (27)$$

where $y^*_{i,1}$ and $y^*_{i,u}$ are related to the compositions of CO_2 in lower and upper channels obtained after the convergence of the previous loop. L_j is the unit segment of the discretized length of the membrane. As the retentate flow rate updates, the pressure within the retentate channel at that stage is calculated using the following relationship:

$$p_{kr} = p_{kr} - \lambda Q_{k_p,\,i}L_j \quad (28)$$

These equations are solved together for each stage and then integrated along the length of the membranes. The result of the current loop is to go back to loop 1 for checking the convergence criteria on pressure drop, which is the maximum error tolerance of 0.001. If the calculation converged loop 1 ends and the final results for flowrates and compositions of retentate and permeate channels become available. However, if the calculations do not converge, they have to reinitialize with updated feed flowrate obtained from immediate values calculated from the previous round of calculations multiplied by the assigned calculated pressure drops:

$$Q_{k_r,\,i\,(updated)} = Q_{k_r,\,i\,(current)} \times \frac{\Delta p_{(assigned)}}{\Delta p_{(calculated)}} \quad (29)$$

The iterative calculations have been performed using programming with MATLAB® software. Then the result of converged calculations has been transferred to Microsoft Excel to be linked with the user-defined Aspen Plus subroutine for demonstration of simulation results. We simulated the investigation of the membrane configuration system with the aid of Aspen Plus ver. 10 software using the Soave-Redlich-Kwong (SRK) equation of state as the base method of calculation. Even though Aspen Plus is a powerful simulation software for chemical processes its model library lacks a membrane separation system, hence we designed and programmed the aforementioned custom membrane model using the "User Model, User 2 subroutine" set for user-defined models in Aspen Plus palette of models. The solution-diffusion model formula together with the data obtained from permeation experiments on different synthesized membranes was introduced in the Microsoft Excel file created for the Aspen-Excel interface. Each of the two membrane blocks has a unique Excel file that is programmed and designed specifically. The needed variables were defined and entered and the calculations and resulting values were entered in Aspen plus created module pages. This data was fed back to the designed Excel file, then our programmed calculations in that Excel file were executed, finally the calculated parameters were reported back to Aspen model pages as the outcome of the simulation. The mentioned defined variables are provided in Table 2.

Table 2. The defined parameters in Aspen plus user model for simulation of the membrane separation system

Variables type	Variable name	Default value
Real	Module area	1.7 m^2
	Selectivity	Depends on MMM
	Effective thickness	0.00001 m
	Δp (pressure drop)	2,000-30,000 Pa
	CH_4 feed composition	0.8-1
	p_h	405,300 Pa
	p_l	101,325 Pa
	Temperature	298.15 K
Integer	Module number	100

Based on the study by Ahmad et al. [28], who completed a techno-economic analysis on different membrane configurations for CO_2/CH_4 separation and concluded that a double step configuration with the recycling of permeate ((DoSRP) is the most optimal design, we decided to select (DoSRP) as the configuration of membrane separation system in Aspen Plus. The process flow diagram of this system is presented in Fig. 6.

The sensitivity analysis was performed in Aspen plus to evaluate the effect of the three most important variables (feed composition, temperature, and thickness of the membranes) on the permeate flux of DoSRP configuration.

RESULTS AND DISCUSSION

1. SEM

The SEM images from the as-synthesized AC particles are presented in Fig. 7.

As it is observable, the particle sizes are mainly in the range of 100-200 nm; however, the particles are not uniform in shape. This can be related to the fact that these particles are synthesized from impure and natural precursors with limitations in yield. No refined precursor is involved in the synthesis procedure, hence the processed, hair, bread, or recycled PET materials with different shapes and ingredients may result in non-uniform AC particle product [29].

The SEM images from the cross sections of all synthesized mixed matrix membrane samples are presented in Fig. 8.

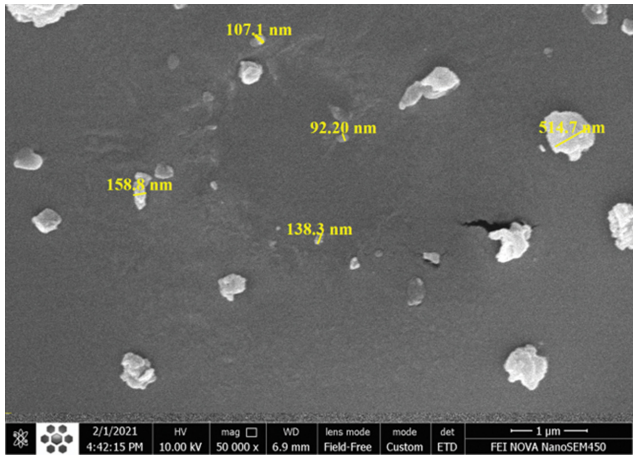

Fig. 7. The SEM images from the synthesized activated carbon particles.

As can be seen in this figure, the compactness of the membranes is observable in all SEM images. This demonstrates that all of the mixed matrix membranes are dense with relatively thick selective layers. The reason for synthesizing thick mixed matrix membranes is to minimize the probability of the creation of defects in the membrane as a result of the possible agglomeration of AC nanoparticles in the matrix of PVA. There is no observable defect at low magnification of SEM images, mainly due to the high thickness of the membrane. The same compactness of the PVA layer can also be observed in other works on PVA membranes synthesized for pervaporation [30,31]. However, for gas separation purposes the defect-freeness of the mixed matrix membrane comprised of particles larger than 100 nm is more critical than those membranes fabricated for pervaporation; hence thicker membranes have been synthesized in this work by increasing the casting blade gap.

The magnified SEM images from the cross-section of the membranes are presented in Fig. 9(a-f).

As can be seen in this figure, there is no significant difference between the sizes of the particles synthesized by three different precursors; however, the aggregation and the dispersion of the AC particles in the matrix of PVA in membranes are different. The sizes of

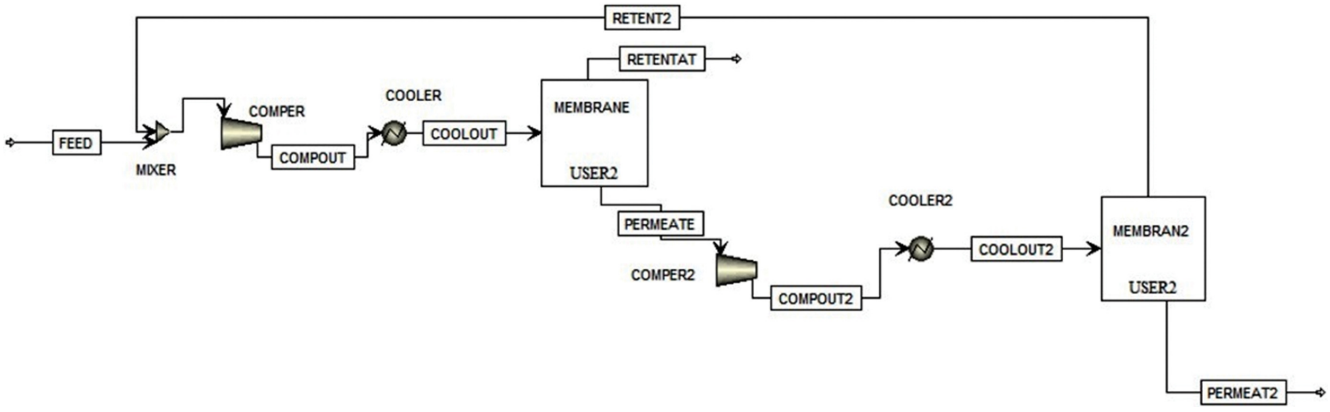

Fig. 6. A process flow diagram of a double step membrane system configuration with permeate recycle.

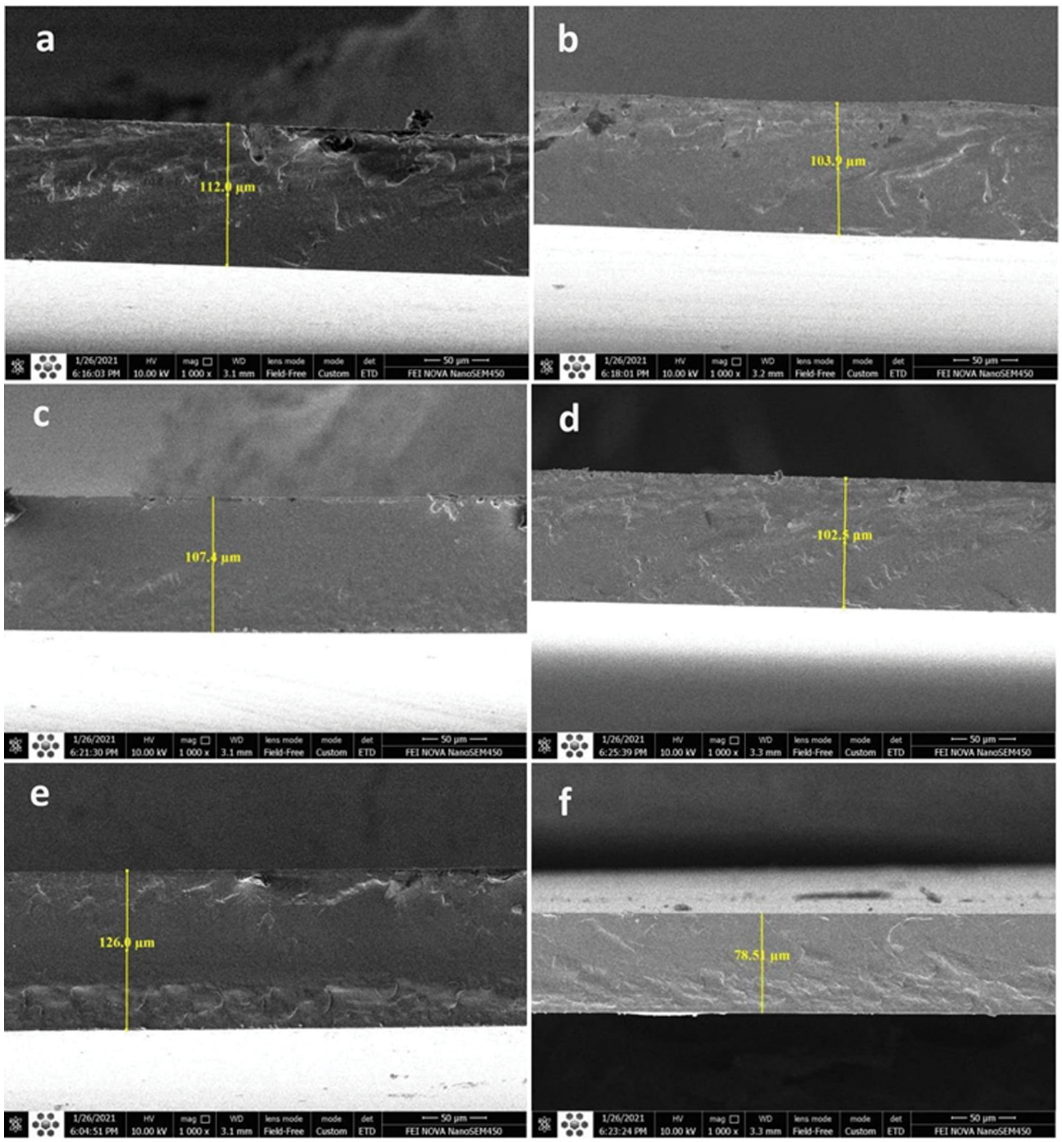

Fig. 8. The wide SEM micrographs from the cross-sections of a) H-AC/PVA-K, b) H-AC/PVA-Z, c) B-AC/PVA-K, d) B-AC/PVA-Z, e) P-AC/PVA-K and f) P-AC/PVA-Z MMM samples.

the isolated single particles in all of the synthesized samples are below 300 nm in all of the synthesized samples, which demonstrates that the adopted approach for the synthesis of particles for incorporation in MMMs is appropriate. The agglomeration of particles that leads to the formation of large bulk of particles is clearer in MMMs synthesized by AC from hair precursors (Fig. 9a and b) and bread precursors (Fig. 9c and d). The agglomeration in Fig. 9e and f, which are related to the AC-MMMs synthesized from PET precursor, is also clear; however, this agglomeration did not result in the formation of large bulk of particles.

This observation in Fig. 9 is somehow backed up by the magnified SEM images from the surfaces of MMM samples (Fig. 10).

As can be seen in this figure, the aggregation of AC particles at the surfaces of samples is clear in all subfigures of Fig. 10. This agglomeration, as was mentioned, is more severe in MMMs synthesized with AC from hair and bread precursors (Fig. 10a, b, c and d). This is mainly because, in the process of AC synthesis from these two precursors, the particles have a higher affinity for agglomeration and form a large bulk of particles. This is also observed in similar work on AC synthesis by Cao et al. [32] and Bal Altuntas et al. [33] in separate research.

2. FTIR

The FTIR spectra of all synthesized MMM samples are provided in Fig. 11.

As can be seen in this graph, the common peaks in all six IR spectra are distinguished by dashed blue colored lines, and the IR peaks specific to KOH-modified and $ZnCl_2$-modified membranes are presented with dashed red lines, The common spectra of all samples from the right to left are at wavenumbers of 1,027, 1,515, 1,720, 2,170, 2,855 and 2,926 cm^{-1} which are, respectively, related to the stretching vibration of C-O in saturated alcohols or the stretching vibration of C-O-C in furans. The emission of H_2O, the stretching

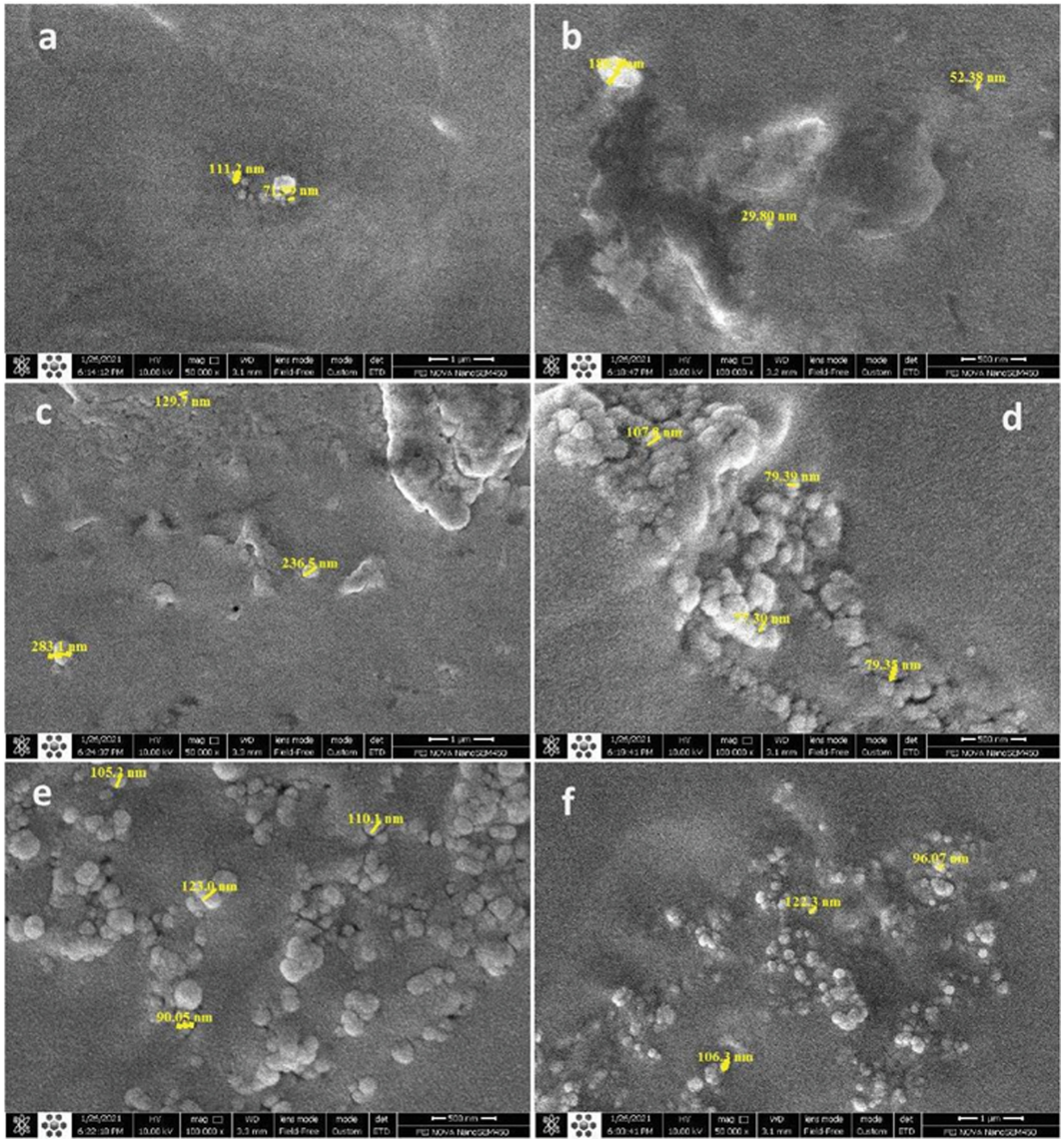

Fig. 9. The SEM micrographs from the magnified cross-sections of a) H-AC/PVA-K, b) H-AC/PVA-Z, c) B-AC/PVA-K, d) B-AC/PVA-Z, e) P-AC/PVA-K and f) P-AC/PVA-Z MMM samples.

vibration of C=C in the aromatic ring, stretching vibration of C=O demonstrating the scission of the vinyl external linkages, the symmetric stretching vibration of C-H and finally the asymmetric stretching vibration of C-H, all related to PVA structure. The peak near around 1,550 cm^{-1} can be related to the hydrates of zinc chloride on exposure to the H_2O molecule in the spectrum which is clear in d, e, and f IR spectra and cannot be observed in a, b, and c IR spectra, which demonstrates that the functionalization of ACs with $ZnCl_2$ was successfully performed (spectra d, e, and f). The peak near 3,450 cm^{-1} is attributed to the stretching vibration of O-H that belongs to H-bonded phenolic OH. This peak is most probably the result of the incorporation of KOH in the functionalization of ACs. This is because it can only be observed in spectra a, b and c, it is absent in spectra d, e, and f. This observation demonstrates the integrity of the functionalization of ACs with the KOH agent.

3. N_2 Adsorption, BET, DFT

The N_2 adsorption-desorption isotherms of MMMs synthesized with ACs modified by KOH along with the DFT pore size distribution of these samples are presented in Fig. 12(a) and (b).

As can be observed in Fig. 12(a), the isotherms of samples prepared with PET and bread precursors are similar to type I and IV of isotherms based on the BDDT classification system, while it resembles type II and IV isotherms for the case of AC samples synthesized with human hair. This demonstrates that the gas molecules were adsorbed in pores in micropore and mesopore regimes and in fact on the external surface of the ACs, respectively.

The variation of the adsorbed N_2 at low partial pressures (p/p_0<0.2-0.3) or, in fact, at the isotherm knees shows that the pore size distribution width in the microporous regime is in this order: P-AC/PVA-K>B-AC/PVA-K>H-AC/PVA-K. This observation is in good agreement with similar work published previously [33].

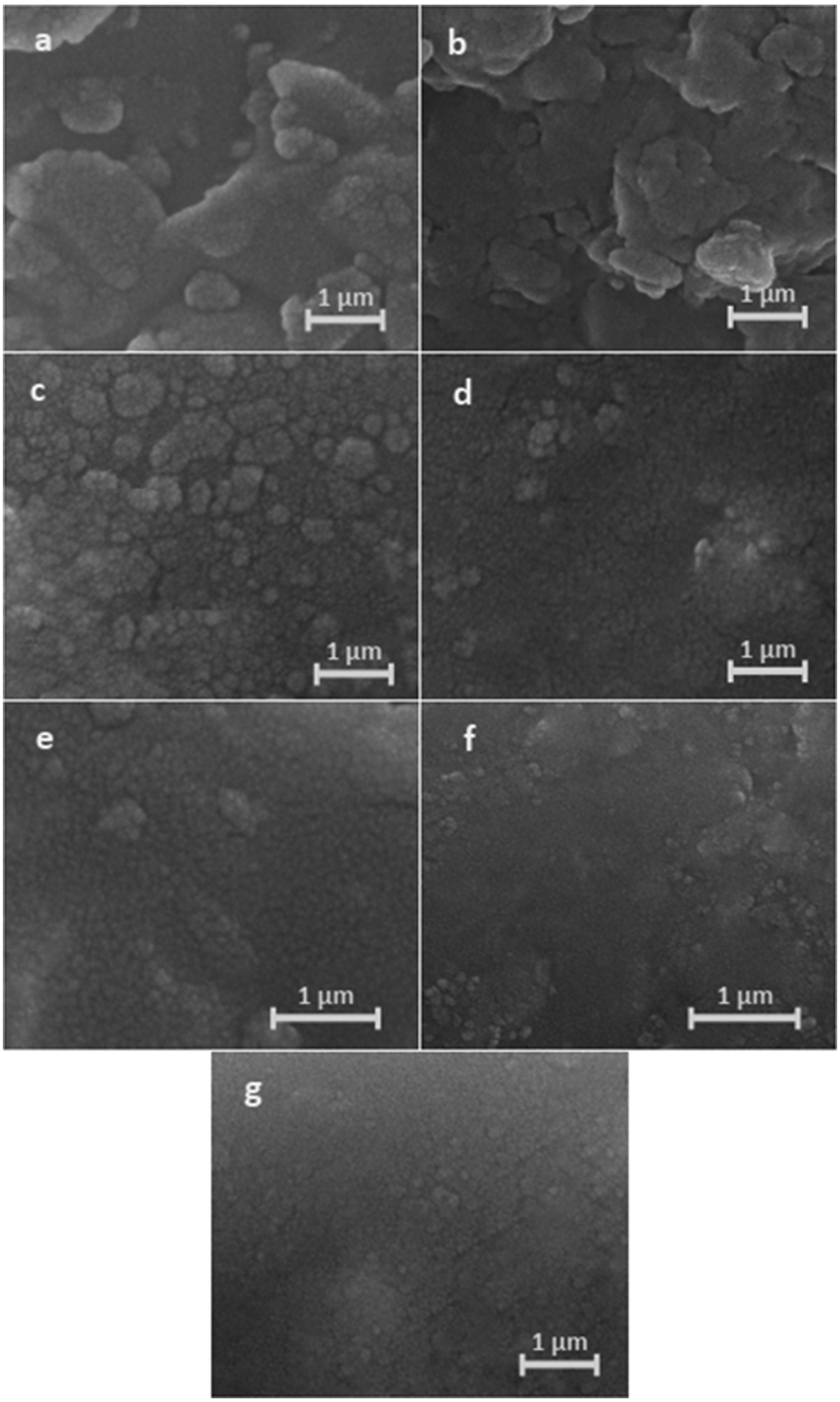

Fig. 10. The magnified SEM micrographs from the surfaces of a) H-AC/PVA-K, b) H-AC/PVA-Z, c) B-AC/PVA-K, d) B-AC/PVA-Z, e) P-AC/PVA-K, f) P-AC/PVA-Z and g) PVA membrane samples.

One of the reasons is that this observation can be related to the more organic nature of human hair compared to bread and PET. The hair consists of large protein molecules, which is the process of calcination, which is removed from the structure of resulted RCP and leaves a larger void compared with bread and PET. Moreover, as can be seen, the maximum sorption capacity of H-AC/PVA-K is lower compared with the other two samples. One reason for this is again related to the relatively lowest numbers of microspores

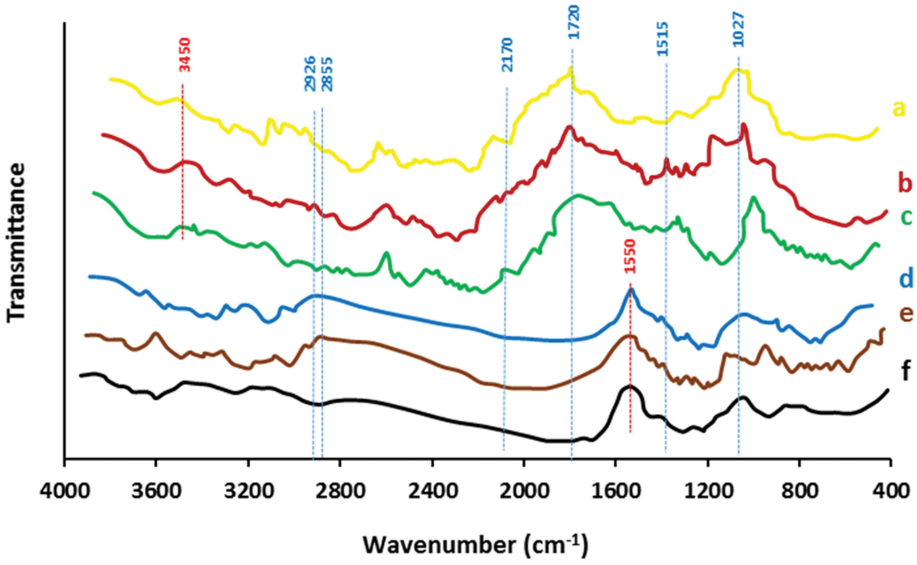

Fig. 11. The FTIR spectra of a) P-AC/PVA-K, b) B-AC/PVA-K, c) H-AC/PVA-K, d) P-AC/PVA-Z, e) B-AC/PVA-Z and f) H-AC/PVA-Z MMM samples.

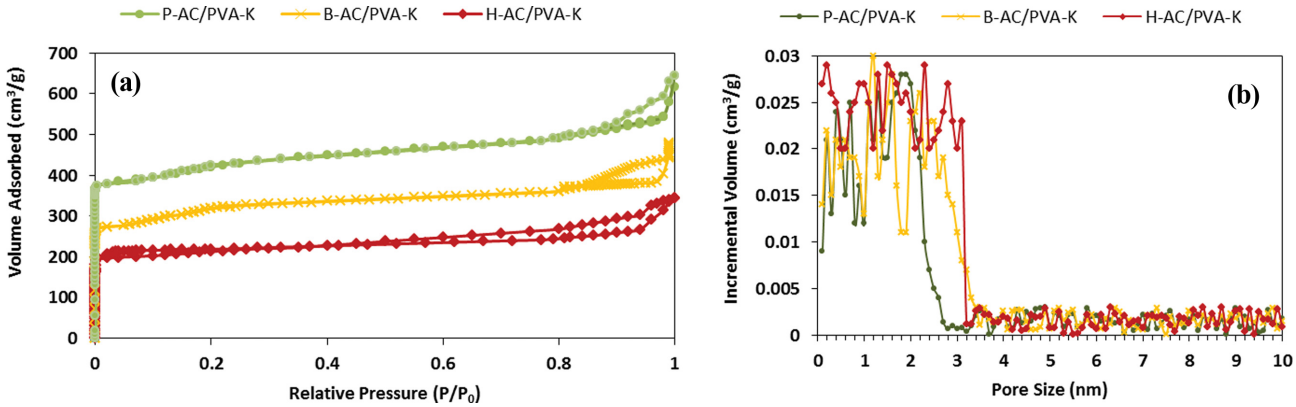

Fig. 12. (a) N_2 adsorption-desorption isotherms and (b) DFT pore size distribution of P-AC/PVA-K, B-AC/PVA-K, H-AC/PVA-K membrane samples.

in the pore structure of AC synthesized from hair. The other is related to the fact that the aggregation of ACs resulting from hair is far more severe compared with the other two samples. This aggregation results in larger particles with lower accessible surface areas and pores for the adsorption of gases, leading to the decline in the sorption capacity of the final AC product.

The DFT pore size distributions of P-AC/PVA-K, B-AC/PVA-K and H-AC/PVA-K samples (Fig. 12(b)) are in good agreement with the N_2 adsorption and desorption isotherms. As can be seen, the majority of the pore volume of MMMs is related to the pores with sizes below 3.2 nm. This means that the majority of pores in all three samples are in the microporous or early mesoporous regime; however, the sample prepared with hair shows generally larger pore sizes in these regimes compared with the other two samples.

The results of N_2 adsorption-desorption analysis and DFT pore size distribution of samples synthesized with AC modified with $ZnCl_2$ are presented in Fig. 13.

As can be seen, again the sample prepared with PET shows the highest sorption capacity, then the sample prepared with bread follows, and the sample prepared with hair shows the lowest sorption capacity amount of the three samples. This observation is in good agreement with the result of N_2 adsorption analysis of MMMs modified with KOH, and it explicitly demonstrates that the type of precursor in the synthesis of ACs is more effective in the sorption capacity of MMMs than the type of functionalization agent. One of the most noticeable and important differences between N_2 adsorption isotherms of samples activated with $ZnCl_2$ and KOH (comparison of Fig. 12(a) and Fig. 13(a)) is the type of hysteresis that emerged. As can be seen in Fig. 12(a), the hysteresis of adsorption isotherms is more similar to type H4, which demonstrates that the pores in samples modified with $ZnCl_2$ are slit-like for which the AC-N_2 pair yields a type II isotherm. This is because in the process of activation, $ZnCl_2$ removes oxygen and hydrogen atoms from water in the compound of carbon precursor and receives no oxygen from organic precursor, and this causes narrow pore formation and an increase in carbon content. For the case of activation

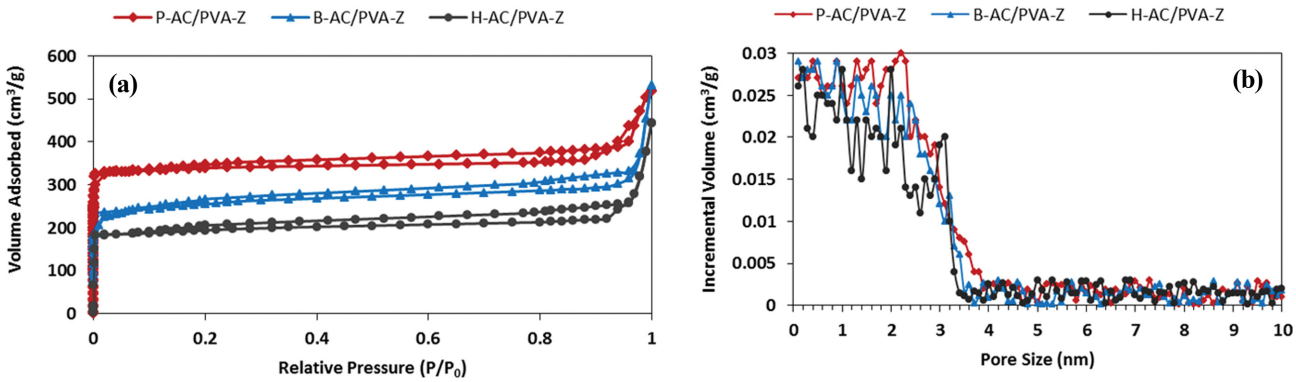

Fig. 13. (a) N_2 adsorption-desorption isotherms and (b) DFT pore size distribution of P-AC/PVA-Z, B-AC/PVA-Z, H-AC/PVA-Z membrane samples.

Table 3. Some textural properties of all synthesized MMMs extracted from adsorption analysis

Code names of membranes	BET (m^2/g)	Pore volume (ml/g)	Mean pore size (nm)
H-AC/PVA-Z	433	0.397	2.5
B-AC/PVA-Z	1,710	0.855	2.2
P-AC/PVA-Z	1,994	1.022	1.9
H-AC/PVA-K	467	0.411	2.4
B-AC/PVA-K	1,823	0.914	2.1
P-AC/PVA-K	2,092	1.140	1.8

with KOH, a more-like H2 type of hysteresis was observed, which demonstrates the presence of pores with narrow and wide sections and possible interconnecting channels. This is in good agreement with the results obtained in some previous similar works. It appears that by activation using KOH, AC with a heterogeneous porosity in the regions of macro-, meso-, and micropores are prepared.

The result of the DFT pore size distribution (Fig. 13(b)) is in good agreement with the result of the N_2 adsorption analysis. As can be seen, the majority of the volume of the pores is from pores sized below 4 nm. This demonstrates the dominance of the micro-meso pore regime in the pore structure of MMMs with ACs activated by $ZnCl_2$.

A summary of the textural properties of synthesized MMMs is provided in Table 3.

As can be seen in Table 3, the BET surface area for MMMs synthesized by ACs prepared from PET and bread is far superior to those prepared with human hair. The reason can be related to the fact that the percentage of mesopores in the pore structure of H-AC/PVA-K and H-AC/PVA-Z is significantly higher compared with other types of synthesized MMMs. This causes an increase in mean pore size and a decrease in the pore volume of the entire membrane, and finally the BET surface area for adsorption. Also, the pore size of the membranes synthesized with ACs activated by $ZnCl_2$ is generally larger compared with those activated with KOH. This is related to the fact that the $ZnCl_2$ medium consists of the total volumes of micro- and mesopores which occur during activation [33], which has not been the case for the KOH medium.

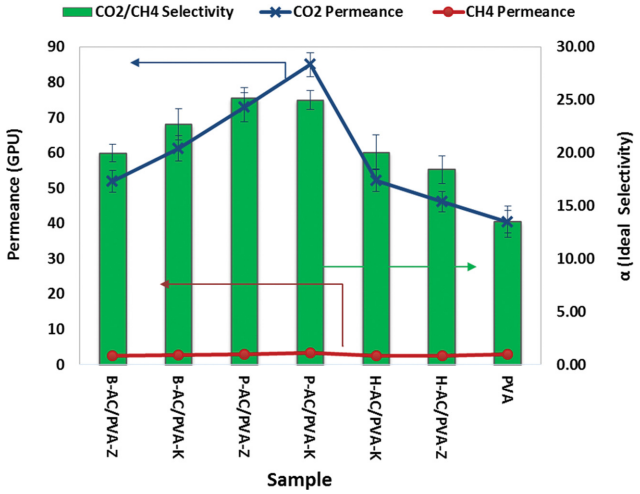

Fig. 14. CO_2 and CH_4 permeances and CO_2/CH_4 permselectivity for all synthesized MMMs and pure PVA membrane at the temperature of 30 °C and pressure of 2 atm.

4. Gas Permeation Results

The results of CO_2 and CH_4 permeation experiments for all of the synthesized membranes are presented in Fig. 14.

As can be seen, the CO_2 permeances of all synthesized MMM samples are higher than that of pure PVA membranes. Moreover, the CO_2/CH_4 ideal selectivity of all samples is higher than that of the PVA membrane. This indicates that the incorporation of ACs in the matrix of PVA was remarkably effective in boosting the CO_2/CH_4 separation performance of the resultung MMMs. Among all MMMs, P-AC/PVA-K and P-AC/PVA-Z samples showed superior CO_2/CH_4 separation performance. This is mainly because the sorption capacity of the membrane synthesized from ACs fabricated from PET is considerably higher than that of two other types of MMMs. This provides more adsorption sites for CO_2, which is a very condensable and soluble gas in both AC and PVA and boosts the solubility and consequently the permeance of this gas through the membrane. For the case of CH_4 which is a larger and significantly less condensable gas than CO_2, the enhanced pore volume and surface area for sorption do not add a significant advantage for permeance increase. Therefore, it is observed that the ideal selec-

tivity for MMMs with higher CO_2 permeance is higher. The other noteworthy point in this figure is that the MMMs with ACs activated with KOH showed slightly better separation performance compared with those activated with $ZnCl_2$. The reason for this observation is that the hydroxyl functional groups on the surfaces of ACs have a superior affinity for CO_2 sorption than that of the chloride group at the same position and condition. Hence the permeance of CO_2 increases with the incorporation of basic activating groups such as KOH.

The results of permeation tests at several different temperatures can be observed in Table S1 (see the supplementary file, Table S1). These data were used to calculate the activation energy for the permeation of CO_2 and CH_4 through the membrane. The calculated activation energies were used in the data fitting method using data sets of Table S1 to determine the fitted values in Table S2 (also see supplementary file).

5. Modeling Validation and Results

5-1. Model Validation

The proposed model for the determination of flowrates and compositions of permeate and retentate streams was validated using the experimental and modeling data of the Pan study in 1986 [34]. The validation of the model is performed by comparing the outlet permeate mole fraction for CO_2 and CH_4 concerning the stage cut for each of the tested gases (Fig. 15(a) and (b)).

Table 4. Comparison of current model accuracy with similar published works based on the calculated percentage of error in the prediction of CO_2 composition in the permeate stream

Stage cut	Error %, Ahamad et al. [28]	Error %, Ahamad et al. [35]	Error %, This Work
0.42	4.39	1.69	0.05
0.45	4.44	1.22	0.34
0.47	4.49	1.35	1.06
0.50	6.89	1.39	3.42
0.55	---	1.20	2.55
0.6	---	1.76	5.89

As can be observed, there is a good agreement between our proposed model with the experimental and modeling data reported by Pan. The percentage error of our model concerning the experimental data of Pan work for CO_2 permeate composition measurement and modeling is compared with the percentage error of two separate studies by Ahamad et al. [28,35], who proposed an approach based on the solution-diffusion model for the prediction of the permeation parameter of hollow fiber membranes in different membrane configurations (Table 4).

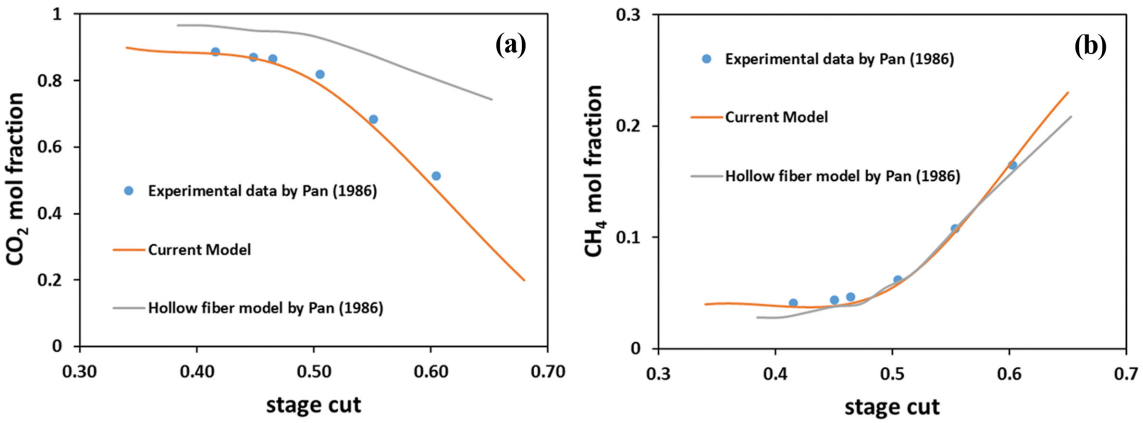

Fig. 15. The accuracy of the proposed model in the prediction of experimental permeation results of work by Pan [34] in comparison to the model proposed by him. for (a) CO_2 and (b) CH_4.

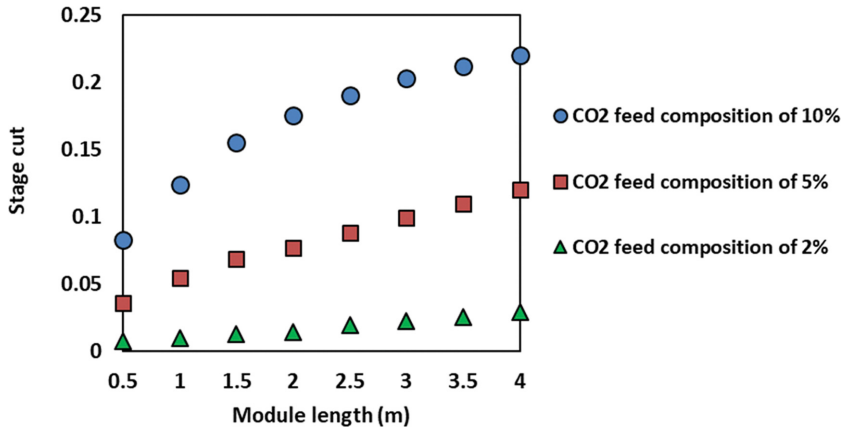

Fig. 16. Stage cut versus module length for (P-AC/PVA-K) with different hypothetical CO_2 content in the feed.

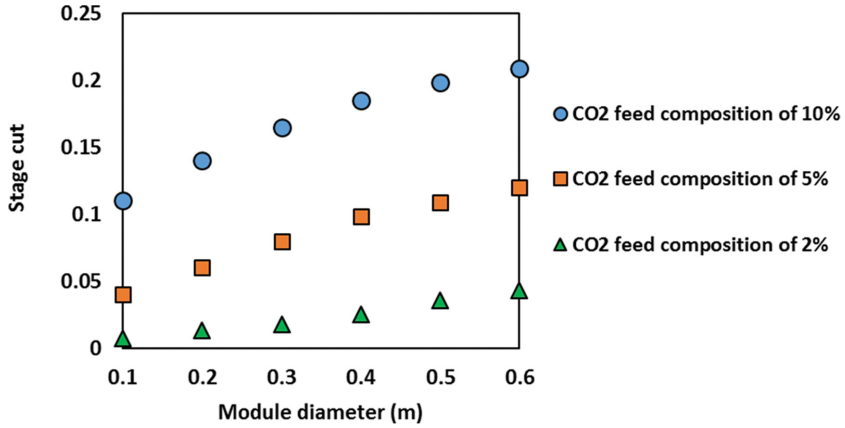

Fig. 17. Stage cut versus module diameter for (P-AC/PVA-K) with different hypothetical CO_2 content in the feed.

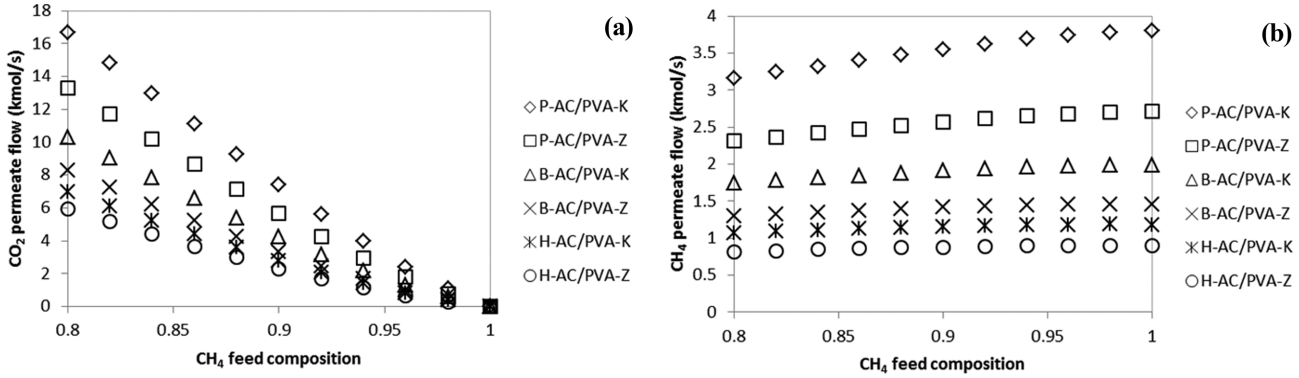

Fig. 18. The effect MMMs feed composition on (a) CO_2 permeate flow rate and (b) CH_4 permeate flow rate in DoSRP configuration.

As is observable, the accuracy of our model is significantly better than the proposed model by Ahmad et al. [28] and is comparable with the accuracy of the model proposed by Ahmad et al. [35], which means that this model can also be a proper tool for evaluation of membrane system configurations.

5-2. Modeling and Simulation Results

The stage cut of best-performed membrane sample (P-AC/PVA-K) was depicted with respect to the hypothetical module length in Fig. 16 for three mixed gas feeds with different CO_2 content.

As can be seen, with the increase in length of the membrane module the stage cut increases, mainly due to the increase in total accessible membrane area for permeation of CO_2. The rate of this increase in lower module length is more significant than in higher ones, which causes the observation of the nearly logarithmic shape of the graphs. This is because the percentage of increase of module length in lower length is significantly larger than that in higher length. For instance, an increase in length from 0.5 to 1 m means 100% length increase, while an increase in length from 3.5 to 4 m means only 14% increase in the length of the module. Also, as the CO_2 content of the feed increases, the stage cut improves, which is expected because the increase in CO_2 permeate flow rate is directly related to the CO_2 content of the feed. The same trend of change in stage cut with the increase in CO_2 content of the feed is also observed in the study of Ahmad et al. [35] on the simulation of gas separation by hollow fiber membranes.

The increase in module diameter shows a similar effect as module length on the stage cut of the module as shown in Fig. 17. This is because of the increase in total accessible membrane area for permeation with the increase in module diameter. It is noteworthy that if we compare Fig. 16 and Fig. 17 with each other, it can be seen that the increase in small value in module diameter is as effective as the increase in large value in module length. This suggests that in order to enhance the stage cut of the whole membrane separation process, it is more logical to roll more flat sheet membranes over each other than fabricating larger flat sheet membranes.

The influence of the feed composition on both CH_4 and CO_2 flow rates of permeate for the designed DoSRP configuration is shown in Fig. 18(a) and (b) for all membranes prepared.

As is observable, with the increase in the CH_4 concentration of the feed, CH_4 permeate flow rate increases while the CO_2 permeate flow rate decreases. The important point extractable from this figure is that the rate of decrease in the CO_2 flow rate with the change in the composition of the feed is more noticeable than the slight increase in CH_4 flow rate. It is because all of the membranes prepared in this work are PVA-based and show a high affinity for CO_2 sorption; therefore, the decrease in the CO_2 concentration of the feed is more sensible for CO_2 permeation than CH_4 permeation.

On the other hand, the percentage change in the content of CH_4 in the feed is 25% in its maximum value; however, this number is 100% for the case of CO_2 content percentage. This is consid-

ered to be the second reason for the drastic drop in the CO_2 flow rate of permeate and a slight rise in permeate flow rate of CH_4.

Also, with multi-step configurations that have a recycle, especially having to recycle of permeate when the feed content approaches close to pure CH_4, the recovery of CH_4 increases substantially; hence, for near pure CH_4 feed composition the DoSRP is favored. The reason is related to the amount of CH_4 that is recycled back to the feed, and because the membrane effective area in this work has a value of 1.7 m^2 and the number of hypothetical membrane modules is not very high (100), the recycle of permeate has a noticeable effect on CH_4 recovery since larger flowrates of CH_4 are transferred back to the feed [36]. Also, from comparing all data samples together it can be said that the membrane with higher permeance and lower selectivity is favored as long as the CH_4 concentration in the feed is high and, as it is clear, the highest CH_4 permeate flow rates is related to (P-AC/PVA-K) sample with the highest permeance for both gases and lowest selectivity.

Fig. 19 shows the effect of temperature on permeate flow rates of CO_2 and CH_4 in DoSRP configuration for all of the membranes synthesized in this work.

As can be seen, the temperature increment causes an increase in permeate flow rates of CO_2 and CH_4 for all synthesized MMMs in the DoSRP configuration. This is because of the notably enhanced flexibility of vinyl chains of PVA which presents excess fractional free volume for both gases to diffuse, which increases the permeance of all MMMs [37]. Besides, as can be observed, the changing rate of CO_2 and CH_4 flow with temperature is higher for MMMs with higher permeance and lower selectivity. This is because the CO_2 and CH_4 permeance of MMMs having higher values of E_p is more dependent on temperature fluctuation. Therefore, it was observed that the MMMs with larger E_p values are more sensible MMMs to the temperature. Moreover, as can be seen in Eqs. (12)-(14), the viscosity of the gas mixture is directly related to the temperature; therefore, the rise in temperature causes a rise in gas viscosity.

It is important to mention that the separation performance of DoSRP configuration for all MMMs significantly deteriorated with the temperature rise. In fact, at 373 K, the value of CH_4 and CO_2 permeate flow rates approached together for the majority of the MMMs simulated. This means that at 373 K, which is a relatively high temperature, the performance of membranes and consequently the DoSRP membrane system declined significantly, leading to the ineffectiveness of the separation process. The effect of the thickness of the AC/PVA mixed matrix membranes on permeate flow rates of CO_2 and CH_4 for simulated DoSRP system is depicted in Fig. 20(a)-(b) for membranes synthesized.

As can be seen in this figure, when the thickness of MMMs increases, the CO_2 permeate flow rate remarkably drops for all MMMs in DoSRP system. This is because the increase in the thickness of MMMs leads to a decrease in permeance of all penetrants, which is logical and also observable; however, because all MMMs

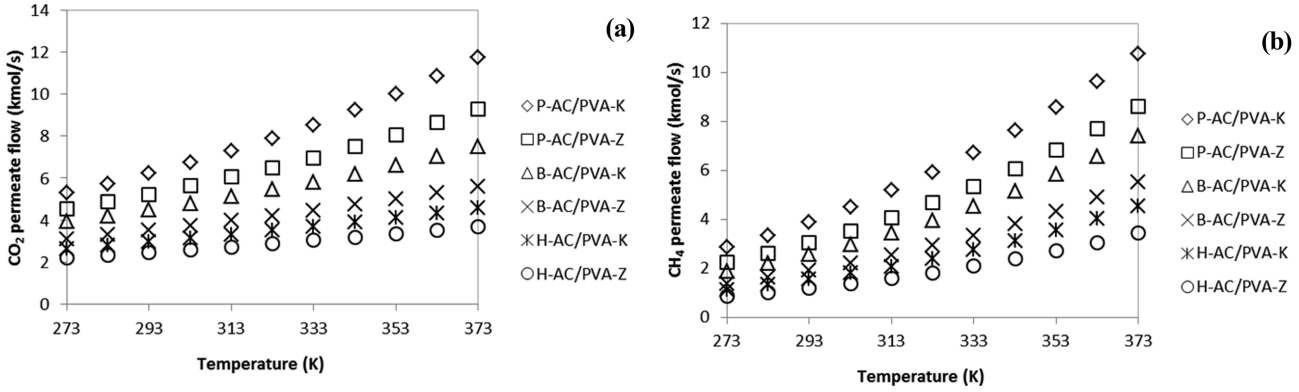

Fig. 19. The simulated effect of temperature on (a) CO_2 permeate flow rate and (b) CH_4 permeate flow rate in DoSRP configuration.

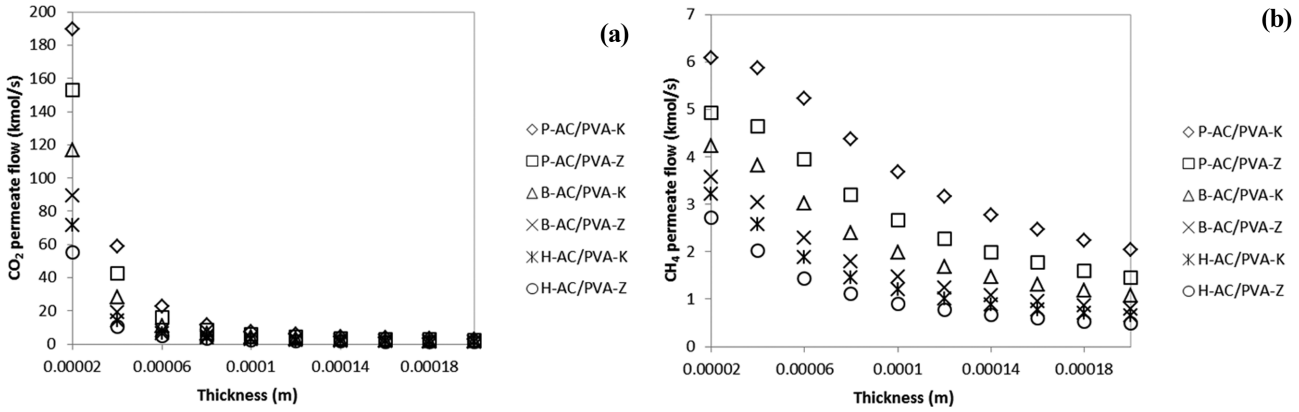

Fig. 20. The effect of membrane thickness on (a) CO_2 and (b) CH_4 permeate flow rates in DoSRP configuration.

in this work show a strong affinity for CO_2 sorption, the effect of membrane thickness is more severe on the decline of the permeate flow rate of CO_2 than that of CH_4. Furthermore, there is a huge difference between the increase in thickness of membrane in thin membranes and thick membranes; for instance, a 30 μm to 90 μm increase in thickness means a 200% increase, while 90 μm to 120 μm means only a 33% increase in thickness of membranes. This percentage drops substantially when the thickness increases slightly; hence it can be said that the flowrate changes in thinner membranes are more intense than that in thicker membranes.

As it can be deduced when the membranes are synthesized with the minimum possible thickness, the membranes with higher permeance show more effectiveness when the recycling of permeate applies. However, with the increase in the thickness of membranes, the DoSRP configuration favors more selective membranes, and these types of membranes show better CO_2/CH_4 separation performance [28]. From this Aspen Plus sensitivity analysis it can be deduced that to achieve a remarkable separation performance in DoSRP configuration, the membrane has to be synthesized as thin as possible in the condition that the process of synthesis results in a morphologically defect-free membrane.

CONCLUSION

Among all synthesized AC/PVA MMMs in this work from three different municipal wastes, the ones prepared with ACs synthesized from PET bottles showed the highest sorption capacity and smaller pore size. The pore sizes of all synthesized ACs regardless of the type of precursor used were in micro- to mesopore range. The result of permeation experiments showed that the MMMs prepared with ACs synthesized from PET bottles showed the highest CO_2 permeance and CO_2/CH_4 ideal selectivity. The activation of ACs using KOH showed more effectiveness in boosting the CO_2/CH_4 separation performance of MMMs compared with that using $ZnCl_2$ due to the presence of CO_2-philic hydroxyl group at the surface of MMMs using KOH activator. Modeling of the spiral wound membrane module converged in three nested loops of calculation to produce the predicted permeate and retentate flow rate values. The validation of the model with previous experimental and modeling data was successful with a maximum parentage error of 5.89%. The simulation of the membrane separation system with Aspen Plus showed that with the increase in the CH_4 content of the feed, the CO_2 permeate flow rate significantly drops while CH_4 permeate flow rate slightly increases. The temperature rise had an increasing effect on the permeances of both gases; however, with the increase in the thickness of membranes, both CO_2 and CH_4 permeances dropped drastically.

FUNDING

This research did not receive any specific grant from funding agencies in the public, commercial, or not-for-profit sectors.

DECLARATION OF INTERESTS

The authors declare that they have no known competing financial interests or personal relationships that could have appeared to influence the work reported in this paper.

SUPPORTING INFORMATION

Additional information as noted in the text. This information is available via the Internet at http://www.springer.com/chemistry/journal/11814.

REFERENCES

1. H. S. Fami, L. H. Aramyan, S. J. Sijtsema and A. Alambaigi, *Resour. Conserv. Recycl.*, **143**, 154 (2019).
2. S. Esmaeilizadeh, A. Shaghaghi and H. Taghipour, *J. Mater. Cycles Waste Manag.*, **22**, 1284 (2020).
3. A. Nabavi-Pelesaraei, R. Bayat, H. Hosseinzadeh-Bandbafha, H. Afrasyabi and K. Chau, *J. Clean. Prod.*, **148**, 427 (2017).
4. M. Rasapoor, M. Adl and B. Pourazizi, *J. Environ. Manag.*, **184**, 528 (2016).
5. S. M. S. Ardebili, *Renew. Energy*, **154**, 29 (2020).
6. A. Taghizadeh-Alisaraei, S. H. Hosseini, B. Ghobadian and A. Motevali, *Renew. Sustain. Energy Rev.*, **69**, 1100 (2017).
7. W. Gao, M. R. Farahani, M. K. Jamil, M. K. Siddiqui, H. M. A. Siddiqui, M. Imran and R. Rezaee-Manesh, *Pet. Sci. Technol.*, **35**, 183 (2017).
8. S. Elkhalifa, T. Al-Ansari, H. R. Mackey and G. McKay, *Resour. Conserv. Recycl.*, **144**, 310 (2019).
9. A. Jain, R. Balasubramanian and M. P. Srinivasan, *Chem. Eng. J.*, **283**, 789 (2016).
10. J. M. Dias, M. C. M. Alvim-Ferraz, M. F. Almeida, J. Rivera-Utrilla and M. Sánchez-Polo, *J. Environ. Manag.*, **85**, 833 (2007).
11. X. Zhang, B. Gao, A. E. Creamer, C. Cao and Y. Li, *J. Hazard. Mater.*, **338**, 102 (2017).
12. S. A. A. Mansoori, Z. Reza, H. Mohammad, M. S. Mohammad, J. Abolfazl, S. Sadegh and E. Akbar, *Nat. Gas Ind. B.*, **9**, 318 (2022).
13. W. Fam, J. Mansouri, H. Li and V. Chen, *J. Membr. Sci.*, **537**, 54 (2017).
14. J. Kim, Q. Fu, K. Xie, J. M. P. Scofield, S. E. Kentish and G. G. Qiao, *J. Membr. Sci.*, **515**, 54 (2016).
15. J. Y. Lai and L. H. Ngu, *IOP Conf. Ser. Mater. Sci. Eng.*, **1195** (2021).
16. D. A. Gkika, N. Vordos, J. W. Nolan, A. C. Mitropoulos, E. F. Vansant, P. Cool and J. Braet, *J. Nanoparticle Res.*, **19**, 177 (2017).
17. L. Deng, T.-J. Kim and M.-B. Hägg, *J. Membr. Sci.*, **340**, 154 (2009).
18. M. Barooah and B. Mandal, *J. Membr. Sci.*, **572**, 198 (2019).
19. J. Ø. Torstensen, R. M. L. Helberg, L. Deng, Ø. W. Gregersen and K. Syverud, *Int. J. Greenh. Gas Control*, **81**, 93 (2019).
20. Z. Jahan, M. B. K. Niazi, M.-B. Hägg and Ø. W. Gregersen, *J. Membr. Sci.*, **554**, 275 (2018).
21. G. Guerrero, M.-B. Hägg, G. Kignelman, C. Simon, T. Peters, N. Rival and C. Denonville, *J. Membr. Sci.*, **544**, 161 (2017).
22. Z. Huang, L. Shen, H. Lin, B. Li, C. Chen, Y. Xu, R. Li, M. Zhang and D. Zhao, *J. Membr. Sci.*, **661**, 120949 (2022).
23. Y. Liu, L. Shen, H. Lin, W. Yu, Y. Xu, R. Li, T. Sun and Y. He, *J. Membr. Sci.*, **612**, 118378 (2020).
24. M. Wu, Y. Chen, H. Lin, L. Zhao, L. Shen, R. Li, Y. Xu, H. Hong and Y. He, *Water Res.*, **181**, 115932 (2020).

25. Z. Huang, J. Liu, Y. Liu, Y. Xu, R. Li, H. Hong, L. Shen, H. Lin and B. Q. Liao, *J. Membr. Sci.*, **623**, 119080 (2021).
26. L. Gurreri, A. Tamburini, A. Cipollina, G. Micale and M. Ciofalo, *Desalin. Water Treat.*, **69**, 178 (2017).
27. R. Khalilpour, A. Abbas, Z. Lai and I. Pinnau, *Chem. Eng. Res. Des.*, **91**, 332 (2013).
28. F. Ahmad, K. K. Lau, A. M. Shariff and G. Murshid, *Comput. Chem. Eng.*, **36**, 119 (2012).
29. R. Hoseinzadeh Hesas, W. M. A. Wan Daud, J. N. Sahu and A. Arami-Niya, *J. Anal. Appl. Pyrolysis*, **100**, 1 (2013).
30. M. E. Dmitrenko, A. V. Penkova, A. I. Kuzminova, M. Morshed, M. I. Larionov, H. Alem, A. A. Zolotarev, S. S. Ermakov and D. Roizard, *Appl. Surf. Sci.*, **450**, 527 (2018).
31. D. A. Reino Olegário da Silva, L. C. Bosmuler Zuge and A. de Paula Scheer, *Sep. Purif. Technol.*, **247**, 116852 (2020).
32. J. Cao, Y. Gao and Y. Ma, *Biomass Convers. Biorefinery*, **9**, 521 (2019).
33. D. Bal Altuntaş, V. Nevruzoğlu, M. Dokumacı and Ş. Cam, *Carbon Lett.*, **30**, 307 (2020).
34. C. Y. Pan, *AIChE J.*, **32**, 2020 (1986).
35. F. Ahmad, K. K. Lau, S. S. M. Lock, S. Rafiq, A. U. Khan and M. Lee, *J. Ind. Eng. Chem.*, **21**, 1246 (2015).
36. R. Qi and M. A. Henson, *Comput. Chem. Eng.*, **24**, 2719 (2000).
37. M. R. Dilshad, A. Islam, U. Hamidullah, F. Jamshaid, A. Ahmad, M. T. Z. Butt and A. Ijaz, *Sep. Purif. Technol.*, **210**, 627 (2019).

Supporting Information

Activated carbon from municipal waste for enhanced CO_2/CH_4 membrane separation: Experimental, modeling and simulation

Abolfazl Jomekian*,† and Bahamin Bazooyar**

*Esfarayen University of Technology, Esfarayen, North Khorasan, Iran
**Department of Mechanical, Aerospace and Civil Engineering (MACE), The University of Manchester, Manchester, M13 9PL, UK
(*Received 29 October 2022 • Revised 30 March 2023 • Accepted 8 May 2023*)

Table S1. CO_2 and CH_4 permeances (GPU) in different MMMs at different temperatures

Temperature (K)	H-AC/PVA-Z		B-AC/PVA-Z		P-AC/PVA-Z		H-AC/PVA-K		B-AC/PVA-K		P-AC/PVA-K	
	CO_2	CH_4	CO_2	CH_4	CO_2	CH_4	CO_2	CH_4	CO_2	CH_4	CO_2	CH_4
303	60.2	3.8	74	5.1	87	7.3	56.5	2.9	47.5	2.4	45.5	1.69
313	73	4.2	88	7	115	9.3	58	3.7	55	2.8	48	1.94
323	77	5.4	99	8.1	127	11.6	66	4.3	59	3.4	53	2.23

Table S2. Calculated CO_2 and CH_4 activation energy of permeation for synthesized MMMs

MMM samples	E_P (kJ/mol) for CO_2	E_P (kJ/mol) for CH_4
H-AC/PVA-Z	8.36	14.17
B-AC/PVA-Z	11.69	16.09
P-AC/PVA-Z	13.14	17.23
H-AC/PVA-K	7.88	10.99
B-AC/PVA-K	7.05	10.30
P-AC/PVA-K	6.12	9.83